Journal of Applied Physics

Effect of particle size on the UV pulsed-laser scribing in computational fluid dynamics-based simulations

Kwan-Woo Park and Suck-Joo Na

Citation: J. Appl. Phys. **107**, 113112 (2010); doi: 10.1063/1.3436588
View online: http://dx.doi.org/10.1063/1.3436588
View Table of Contents: http://jap.aip.org/resource/1/JAPIAU/v107/i11
Published by the American Institute of Physics.

Effect of particle size on the UV pulsed-laser scribing in computational fluid dynamics-based simulations

Kwan-Woo Park and Suck-Joo Na[a)]
Department of Mechanical Engineering, KAIST, 355 Gwahangno, Yuseong-Gu, Daejeon 305-701, South Korea

(Received 16 February 2010; accepted 26 April 2010; published online 14 June 2010)

A computational model for UV pulsed-laser scribing of silicon target is presented and compared with experimental results. The experiments were performed with a high-power Q-switched diode-pumped solid state laser which was operated at 355 nm. They were conducted on n-type 500 μm thick silicon wafers. The scribing width and depth were measured using scanning electron microscopy. The model takes into account major physics, such as heat transfer, evaporation, multiple reflections, and Rayleigh scattering. It also considers the attenuation and redistribution of laser energy due to Rayleigh scattering. Especially, the influence of the average particle sizes in the model is mainly investigated. Finally, it is shown that the computational model describing the laser scribing of silicon is valid at an average particle size of about 10 nm. © *2010 American Institute of Physics*. [doi:10.1063/1.3436588]

I. INTRODUCTION

Recently, global warming has been reported to be caused mainly by the overuse of fossil fuels. As a result, researchers around the world are making efforts to develop next-generation energy sources as substitutes for fossil fuels. Among these, solar cells have come into the spotlight as their use has grown rapidly owing to their effectiveness. Among the various solar cells, crystalline silicon solar cells have become the mainstream solution. UV pulsed-laser scribing plays a significant role in the processing of such solar cells.[1]

The UV pulsed-laser scribing is carried out through interaction between the laser and the material, yielding various results depending on which lasers and materials are chosen. Therefore, characterizations of the materials to be used should be fully understood and a suitable laser source should be chosen before processing. It is the interaction between the material and the laser beam that informs such choices. This is because the interaction involves the absorption process of the laser beam into the material, and decides the quantity of the absorbed light. Consequently, it significantly affects the material shape and process efficiency.

As mentioned above, the absorption of the laser beam has great significance. When a laser beam is irradiated to the material in the UV pulsed-laser scribing process, the absorption quantity of the laser beam is decided by intrinsic and extrinsic factors. Namely, intrinsic factors include the change in electrical conductivity according to the increase in temperature. Several extrinsic factors include the multiple reflection effect induced by the formation of keyholes; the Rayleigh absorption-scattering effect caused by the formation of particles; and the inverse Bremsstrahlung effect produced by plasma, among others.[2–4]

In the process, absorption increases rapidly because of the multiple reflection effect, an extrinsic factor, over the melting point. The temperature keeps rising to the boiling point and above, and then absorption of the laser beam is influenced by not only the multiple reflection effect but also the Rayleigh absorption-scattering effect. Absorption shows a tendency to decrease again due to the Rayleigh absorption-scattering effect. In this process, the inverse Bremsstrahlung effect is negligible, because the laser-induced plasma effects are not dominant. However, in the process, absorption is greatly influenced by the above mentioned two extrinsic factors. In other words, physical interactions like multiple reflections and Rayleigh absorption-scattering, which play a crucial role in laser beam absorption, should be understood in order to carry out the UV pulsed-laser scribing process effectively.

In this article, a UV pulsed-laser scribing model including multiple reflections and Rayleigh absorption-scattering effects will be suggested. Especially, the scattering parameter such as a particle size will be investigated in detail. The results from the computational model will be compared with experimental observations.

II. EXPERIMENTAL PROCEDURE

A high-power Q-switched diode-pumped solid state laser (DPSSL) scribing was conducted on n-type silicon wafer, which was chosen to be applied to a solar cell edge isolation. The silicon wafer had a thickness of 500 μm; its physical properties are listed in Table I. The laser was operated at 355 nm. The maximum average power was 8 W. The pulse repetition rates varied from 5 to 250 kHz. Consequently, the pulse width ranged from 80 to 135 ns. A galvanometer scanner and 109 mm f-theta focusing optic were used for the UV pulsed-laser scribing. The direct writing method with a focused laser beam was used. The transverse electromagnetic mode was TEM_{00}, which was a near-Gaussian profile. The minimum waist of the beam was around 7.5 μm. The scribing was conducted at the room temperature without assistant gas. Figure 1 shows the schematic of the whole setup.

[a)]Electronic mail: sjna@kaist.ac.kr.

TABLE I. Data used for simulations. See Refs. 10–12.

Property	Value (unit)
Melting temperature	1683 (K)
Boiling temperature	3514 (K)
Liquid density	2.52 (g/cm^3)
Solid density	2.32 (g/cm^3)
Surface tension	730 (erg/cm^2)
Liquid specific heat	1.0×10^7 (erg/g K)
Solid specific heat	7.0×10^6 (erg/g K)
Liquid thermal conductivity	1.48×10^7 (erg/s cm K)
Solid thermal conductivity	2.21×10^6 (erg/s cm K)
Latent heat of fusion	1.797×10^{10} (erg/g)
Dynamic viscosity	0.007 56 (P)

Several experiments have been performed to find the best working conditions. Adjustable parameters such as laser power, pulse repetition rate, and scribing speed have been varied to investigate their influences on the work piece surface. The laser pulse repetition rate, spot diameter, and the vector scanning speed determine the overlap, which deeply affects the scribing quality. Figure 2 shows the relationship. The overlap rate is normalized in units of R_o

$$R_o = \left(1 - \frac{v}{d \times R_p}\right) \times 100(\%), \tag{1}$$

where v is the scribing speed (mm/s), d is the spot diameter (mm), and R_p is the pulse repetition rate (Hz).

III. MATHEMATICAL APPROACH

A. GOVERNING EQUATIONS AND BOUNDARY CONDITIONS

In this study, volume of fluid method[5] was used to analyze a groove shape of UV pulsed-laser scribing. The computational fluid is assumed as a Newtonian, incompressible and laminar flow. It then basically follows three governing equations: the continuity, momentum, and energy equations. The scribing process is supposed to occur in a Cartesian coordinates system for a three-dimensional (3D) space. The boundary conditions are expressed below. The laser beam is assumed to have a Gaussian intensity distribution, and considered as a surface heat flux boundary condition. The Gaussian beam is given by

$$q_L(x,y,z) = \frac{2Q}{\pi r_L^2}\exp\left(-2\frac{x^2+y^2}{r_L^2}\right). \tag{2}$$

Here, Q is the laser power, In addition, the laser beam is assumed to have a divergence, which can be modeled as follows:

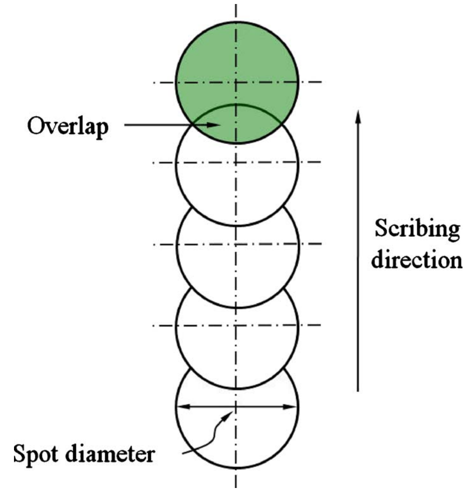

FIG. 2. (Color online) Overlap process of the laser scribing of silicon.

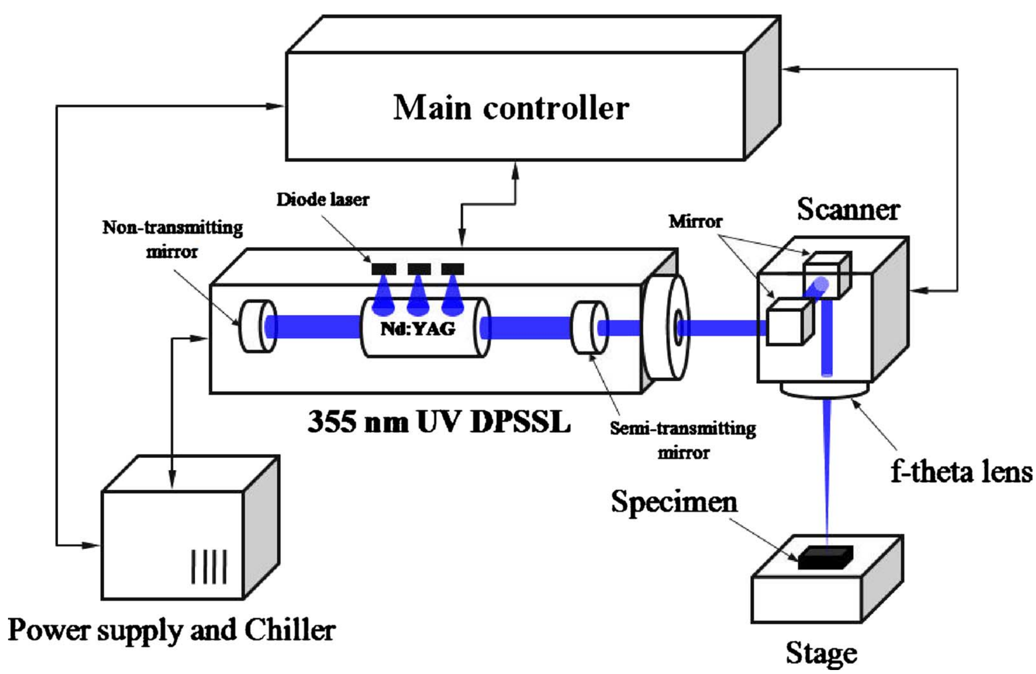

FIG. 1. (Color online) Experimental system for the laser scribing of silicon.

$$r_L = r_0 + M^2 \frac{\lambda}{\pi r_0} |z_0 - z|. \tag{3}$$

Here, r_0 is the focal radius, M^2 is the beam-quality factor ($M^2 = 1$ for a Gaussian laser), λ is the wavelength, and z_0 is the focal point on the z axis.

When a high power laser beam is irradiated on the surface, it is well known that the surface temperature reaches rapidly to the melting and even the boiling point of the material. This induces a recoil pressure. The recoil pressure represents the repulsive force on the surface produced by the evaporation of material. This force contributes to forming a narrow and deep keyhole shape. A simplified form of this recoil pressure[6] is expressed as follows:

$$P_r \cong 0.54 P_0 \exp\left(L_V \frac{T_S - T_B}{R T_S T_B} \right). \tag{4}$$

Here, P_r is the recoil pressure, P_0 is the atmospheric pressure, L_V is the latent heat of vaporization, R is the gas constant, T_S is the solidus temperature, and T_B is the boiling temperature.

The boundary condition for the top surface contains the surface heat flux considering the laser heat source, while the pressure boundary condition is given by the recoil pressure. Accordingly, the boundary conditions for the heat and pressure can be expressed as follows:

$$K \frac{\partial T}{\partial n} = F_q - h_A (T - T_\infty) - \sigma_s \varepsilon_r (T^4 - T_\infty^4) - q_{vap}, \tag{5}$$

$$-P + 2\mu \frac{\partial V_n}{\partial n} = -P_r + \frac{\gamma}{R}. \tag{6}$$

Here, F_q is the laser surface heat flux, h_A is the convection coefficient, and T_∞ is the temperature of ambient air. σ_s, ε_r, and q_{vap} indicate the Stefan–Boltzmann constant, emissivity, and heat loss caused by vaporization, respectively. The second and third terms of the equations denote the heat losses caused by ambient air convection and heat radiation, respectively. n, γ, and R denote the normal component, the surface tension coefficient, and radius of the surface curvature, respectively.

B. LASER-INDUCED PLUME MODEL

A laser-induced plume, which reduces the laser irradiation to the surface of the workpiece by absorbing and redistributing the beam, can be calculated by applying the scattering theory. The following assumptions were made in the formulation of the laser-induced plume model:

(1) the particle diameters have the size from 1 to 15 nm.
(2) The particles are spherical clusters, and their materials are homogeneous.
(3) The nature of the interaction between electromagnetic waves and particles is determined by the relative size of the particles compared with the wavelength of the radiation. Defining a size parameter:[7]

$$X = \frac{2\pi r}{\lambda}. \tag{7}$$

Here, r is the effective radius of the particle. In this study, the scattering is assumed as Rayleigh scattering because the size parameter is $X \ll 1$.
(4) The volume fraction of particles is less than 0.006. Therefore, the scattering is independent scattering, which is not affected by the presence of surrounding particles. Defining a volume fraction:[8]

$$f_V = \frac{\rho_p \pi d^3}{6}. \tag{8}$$

Here, ρ_p is the number density of particles, and d is the diameter of the particle.
(5) The number density of particles is constant during the simulation.
(6) Evaporating particles do not interact with the groove wall.
(7) Emission in the particles and plasmas are ignored because they have little effect on the attenuation of incident beam in this simulation conditions.

A particle number density is the number of particle per volume. The number density can be calculated by Hertz–Langmuir equation[8] and Sedov's blast wave theory. The Hertz–Langmuir equation is expressed as

$$\Gamma = 5.8 \times 10^{-2} \sqrt{\frac{M}{T}} p \alpha. \tag{9}$$

Here, Γ is the mass evaporation rate, M is the mass of the evaporating molecule, T is temperature ($T \geq$ boiling temperature), p is the vapor pressure, and α is the evaporation coefficient. The total vaporized particle number is calculated as the total mass, which is an integration of Γ over time and surface area, by the particle mass. Sedov's blast wave theory describes the propagation of shock waves after intense explosions. A contact front,[9] which separates the evaporated particles and shocked ambient gas can be derived using the theory. The contact front can be determined as follows:

$$R_{cf} = R_{sf} \frac{2}{\gamma + 1} \left(\frac{t}{t_0} \right)^{2/5[(1-\gamma)(1+\gamma)]} \tag{10}$$

Here, R_{cf} is the contact front distance, R_{sf} is the shock front distance, t is the time, γ is the adiabatic exponent, t_0 is the time of the transition from planar to spherical expansion of the shock wave. Detailed descriptions about these equations were explained in the authors' previous paper (see Ref. 3).

Figure 3 shows the laser pulse incident on the workpiece and the laser-induced plume ejected into the atmosphere with the shock wave propagation. In the figure, the laser beam proceeds in a straight path without reduction until it meets the boundary (contact front) of medium containing small particles (laser-induced plume). After meeting with the contact front, the laser beam is divided into transmitted light (solid line), absorbed light (dot), and scattered light (dashed line). When the transmitted light advances, some of the energy of the transmitted light is absorbed into the workpiece, and the rest of its energy is reflected through multiple reflections

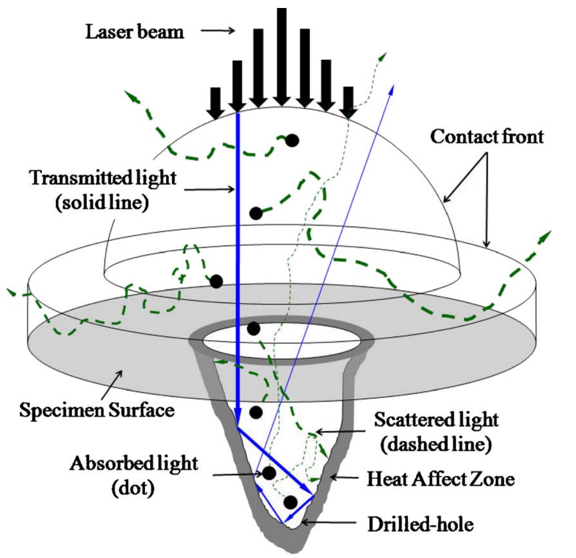

FIG. 3. (Color online) Schematic representation of the transmitted, absorbed, and scattered light in the analysis domain.

according to Fresnel reflection theory. The absorbed light is absorbed into the particles. When the scattered light considering the Rayleigh scattering phase function scatters, some of its energy is absorbed into the workpiece and the rest is scattered into the surroundings. The details of the model will not be given (see Ref. 3). In the case of transmitted light, the increase in the beam path causes the decrease in the input intensity because a lot of particles exist on the beam path. This is explained using the Beer–Lambert's law. It is regarded as

$$I_{tr} = I_o e^{-\alpha_{ext} d}, \tag{11}$$

$$\alpha_{ext} = \alpha_{abs} + \alpha_{sca}. \tag{12}$$

Here, I_o is the laser intensity on the contact front, I_{tr} is the transmitted laser intensity on the workpiece surface, d is the multiple-reflection path distance through the analysis volume, and α_{ext}, α_{abs}, and α_{sca} denote the extinction, absorption, and scattering coefficient, respectively. The scattering coefficient[7] and absorption coefficient[8] are written by

$$\alpha_{sca} = \pi r^2 \rho_p \frac{8}{3}\left[\frac{m^2-1}{m^2+1}\right] X^4, \tag{13}$$

$$\alpha_{abs} = -\pi r^2 \rho_p 4 \,\mathrm{Im}\left\{\frac{m^2-1}{m^2+1}\right\} X. \tag{14}$$

Here, r is the particle radius, ρ_p is the number density of particles, m is the complex index of refraction, and X is the size parameter. As mentioned above, the transmitted light (I_{tr}) travels on the basis of the multiple-reflection algorithm. Absorption takes place as the laser beam penetrates into the particles. The amount of absorption into the particles can be determined as follows:

$$I_{abs} = I_o(1 - e^{-\alpha_{abs} d}). \tag{15}$$

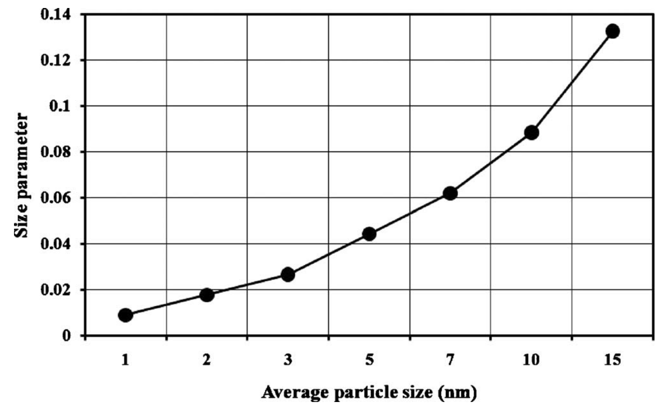

FIG. 4. Size parameter as a function of the particle size.

IV. RESULTS AND DISCUSSION

A user subroutine of the computational fluid dynamics software provided by FLOW-3D has been used to deal with the simulation model on high-power UV Q-switched DPSSL scribing. In order to facilitate the comparison of simulation results for the various cases, the same domain, the same mesh size, and 3D modeling approach were used for all the cases. In the simulation, the laser scribing was conducted on silicon. The laser wavelength was 355 nm. The transverse electromagnetic mode was TEM_{00}. The beam diameter was 15 μm. The laser was set to operate at a repetition rate of 30 kHz and with a pulse width of about 80 ns. The average laser power was set to 5 W. The focal point was on the top surface of the workpiece. The scribing speed was set to 300 mm/s. The overlap rate was 30%. A linelike patterning was achieved. The scribing was conducted at room temperature without assistant gas. Physical properties for the simulation are listed in Table I.

In this study, seven particle sizes (diameter: 1, 2, 3, 5, 7, 10, and 15 nm) are considered. Figure 4 shows the values of particle size parameters as a function of particle size. The particle size parameters are between 0.009 and 0.133. In the case of the 15 nm particle size, the size parameter is a little larger than the others. However, all the cases can be defined as Rayleigh scattering. The volume fractions of particles as a function of particle size are shown in Fig. 5. The volume fractions of particles are less than 0.006. Therefore, all the scatterings in this simulation are independent scattering. In

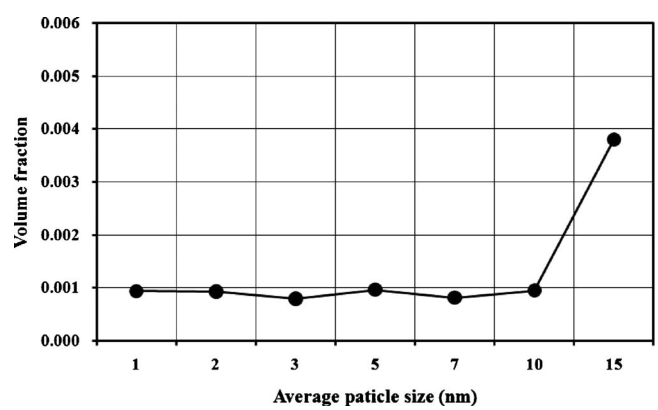

FIG. 5. Volume fraction as a function of the particle size.

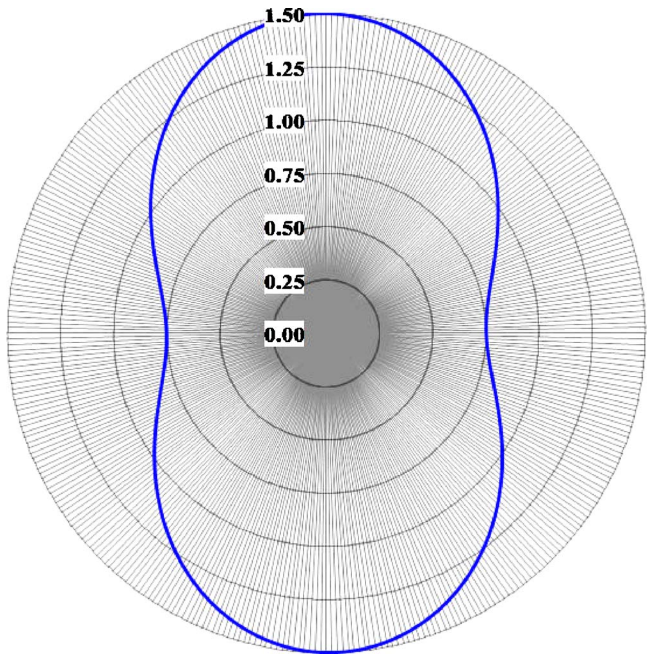

FIG. 6. (Color online) Polar diagram of Rayleigh phase function.

Fig. 5, it is interesting to note that the volume fraction suddenly increases when 15 nm particle size is used. Figure 6 presents the Rayleigh phase function, which is considered in the simulation.[7] The phase function is the same for each particle since the particle shape and size are uniform. The Rayleigh phase function follows:

$$f(\theta) = \frac{3}{4}(1 + \cos^2 \theta), \tag{16}$$

where θ is a scattering angle.

The simulated values of average particle number densities for various particle sizes are presented in Fig. 7. For all particle sizes, the average particle number densities fluctuate with the increase in pulse order. It is clear from Fig. 7 that the particle number density decreases as the particle size goes up. However, it is observed that the particle number density at 15 nm is higher than at 10 nm. Figure 8 shows the dependence of average scattering coefficient on the particle sizes. The scattering coefficient increases exponentially at 15

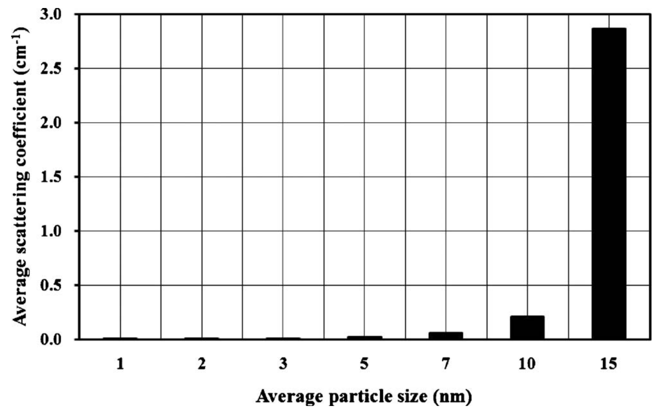

FIG. 8. The variation in average scattering coefficient with particle size.

nm particle size. The increase in scattering coefficient induces absorption of the scattered light to increase. In the workpiece the temperature increases with the absorption. As a result, more particles are generated so that the particle number density at 15 nm is higher than at 10 nm as shown in Fig. 7.

The variation in the absorption energy on the workpiece produced by the transmitted and scattered light is shown in Fig. 9. Figure 9 shows that the scattering light gradually increases from 0.03 to 28 μJ below 15 nm while the value dramatically increases to 581 μJ at 15 nm. As explained above, absorption of the scattered light steeply increases with the increased scattering coefficient at 15 nm. It is observed that the transmitted light varied between 230 and 280 μJ in Fig. 9. The scattering and the absorption coefficients are presented in Figs. 8 and 10 for the different particle sizes. From these two figures, it can be seen that the absorption coefficient is dominant compared with the scattering coefficient. The extinction coefficient is made up of two parts, absorption and scattering. The transmitted light depends on the extinction coefficient. Thus, the absorption coefficient has significant effect on the transmitted light. Eventually, at 15 nm the transmitted light does not steeply increase unlike the scattered light because of a large amount of absorption energy in the particles.

The experimental and the simulated values of scribing width for various particle sizes are presented in Fig. 11. The

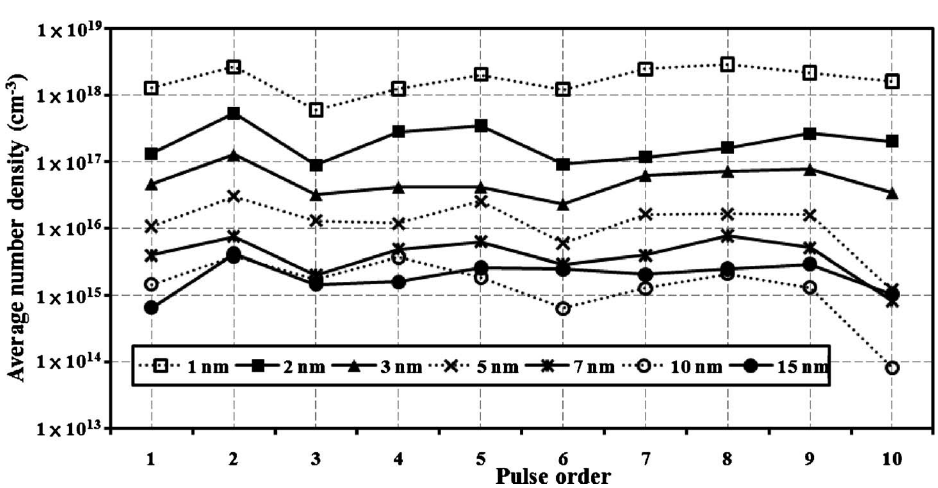

FIG. 7. Average number density of particles vs pulse order for different particle sizes.

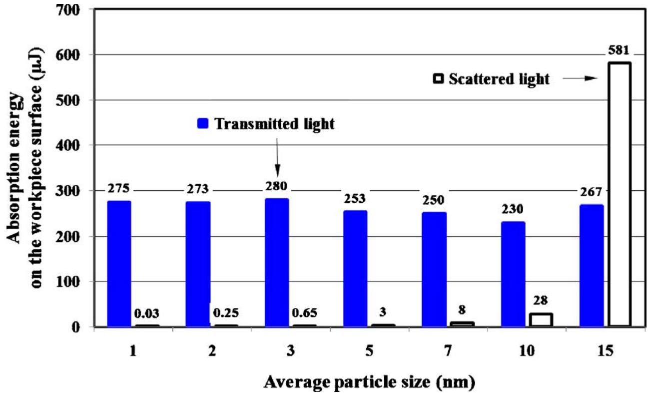

FIG. 9. (Color online) The simulated absorption energy on the workpiece surface as a function of particle size for transmitted and scattered light.

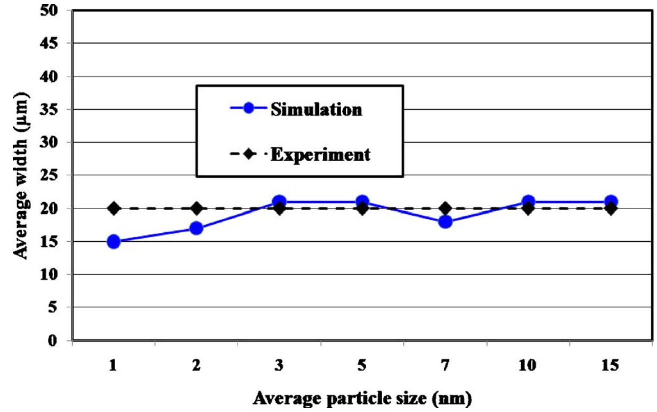

FIG. 11. (Color online) Scribing width as a function of particle size.

width is approximately 20 μm for experiment and varies for simulations between 15 and 21 μm. Figure 12 presents the results for the simulated scribing depth and the experimental scribing depth versus particle size. The simulated scribing depth shows a good agreement with the experimental results below 15 nm. However, there is some difference between the simulated and the experimental value of the scribing depth at 15 nm. In summary, although the seven particles are included in Rayleigh scattering, the value of the scattering coefficient at 15 nm is significantly different from the others. Thus, the selection of particle sizes makes a considerable impact on the Rayleigh scattering effects. Furthermore, it has an effect on the simulated scribing geometry and dimensions.

In this study, it is observed that the simulated scribing geometry and dimensions agree well with the experimental results at 10 nm particle size. Figure 13 shows a comparison of the experimentally determined scribing results with the corresponding numerically computed results at 10 nm.

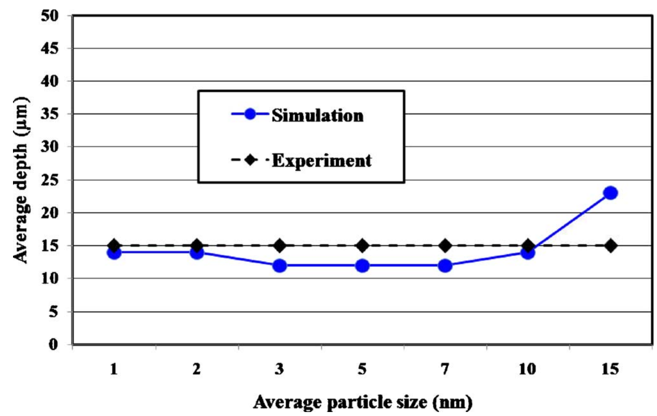

FIG. 12. (Color online) Scribing depth as a function of particle size.

V. CONCLUSIONS

A 3D simulation model including multiple reflections and Rayleigh absorption-scattering effects is presented to study the vaporized particle size effects in the high-power UV Q-switched DPSSL scribing. Simulations are carried out with the seven different particle sizes, which belong in Rayleigh scattering. Various simulation results are obtained. Especially, when the particle size is 15 nm, the scattering co-

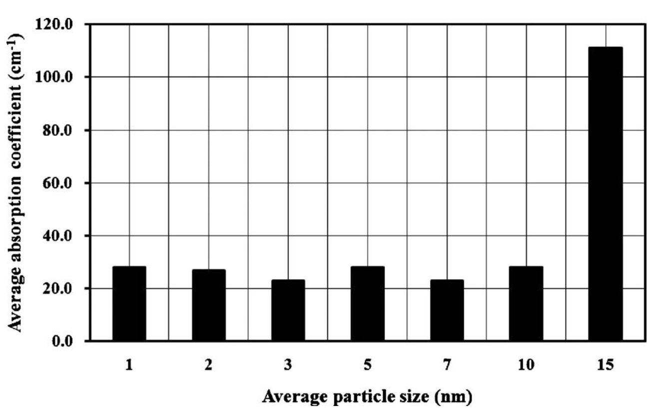

FIG. 10. The variation in average absorption coefficient with particle size.

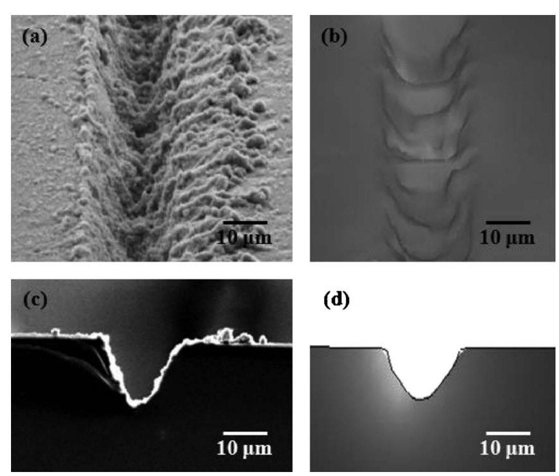

FIG. 13. Comparison of the experimental results [(a) and (c)] and the simulated results [(b) and (d)] at 10 nm: The cross sections are arbitrarily chosen.

efficient suddenly increases. Considering the simulation results, it is highly probable that the selection of particle sizes makes a considerable impact on the Rayleigh scattering effects. Furthermore, it has an effect on the simulated scribing geometry and dimensions. Therefore, in order to obtain a good agreement between the simulated and the experimental results, the particle size should be carefully adjusted. Judging from the simulated results, the average particle size is likely to be about 10 nm in an experiment under the conditions used in this study.

ACKNOWLEDGMENTS

This work was supported by the Brain Korea 21 Project and the National Research Foundation of Korea (NRF) grant funded by the Korea government (MEST) (Grant No. 2009-0085047).

[1] D. M. Karnakis, Appl. Surf. Sci. **252**, 7823 (2006).
[2] M. F. Modest, ASME J. Heat Transfer **128**, 653 (2006).
[3] K. W. Park and S. J. Na, Appl. Surf. Sci. **256**, 2392 (2010).
[4] D. Lacroix, G. Jeandel, and C. Boudot, J. Appl. Phys. **84**, 2443 (1998).
[5] C. W. Hirt and B. D. Nichols, J. Comput. Phys. **39**, 201 (1981).
[6] J. Y. Lee, S. H. Ko, D. F. Farson, and C. D. Yoo, J. Phys. D: Appl. Phys. **35**, 1570 (2002).
[7] M. F. Modest, *Radiative Heat Transfer* (Academic, New York, 2003).
[8] X. He, T. DebRoy, and P. W. Fuerschbach, J. Appl. Phys. **94** 6949 (2003).
[9] G. Callies, P. Berger, and H. Hugel, J. Phys. D: Appl. Phys. **28**, 794 (1995).
[10] S. Y. Chou, C. Keimel, and J. Gu, Nature (London) **417**, 835 (2002).
[11] H. Fujii, T. Matsumoto, S. Izutani, S. Kiguchi, and K. Nogi, Acta Mater. **54**, 1221 (2006).
[12] D. J. Lim, H. Ki, and J. Mazumder, J. Phys. D: Appl. Phys. **39**, 2624 (2006).